Lattice model for self-assembly with application to the formation of cytoskeletal-like structures

Shannon F. Stewman and Aaron R. Dinner*
Department of Chemistry, James Franck Institute, and Institute for Biophysical Dynamics, The University of Chicago, 929 East 57th Street, Chicago, Illinois 60637, USA

(Received 18 July 2006; revised manuscript received 8 March 2007; published 11 July 2007)

We introduce a stochastic approach for self-assembly in systems far from equilibrium. The building blocks are represented by a lattice of discrete variables (Potts-like spins), and physically meaningful mechanisms are obtained by restricting transitions through spatially local rules based on experimental data. We use the method to study nucleation of filopodia-like bundles in a system consisting of purified actin, fascin, actin-related protein 2/3, and beads coated with Wiskott-Aldrich syndrome protein. Consistent with previous speculation based on static experimental images, we find that bundles derive from Λ-precursor-like patterns of spins on the lattice. The ratcheting of the actin network relative to the surface that represents beads plays an important role in determining the number and orientation of bundles due to the fact that branching is the primary means for generating barbed ends pointed in directions that allow rapid filament growth. By enabling the *de novo* formation of coexisting morphologies without the computational cost of explicit representation of proteins, the approach introduced complements earlier models of cytoskeletal behavior *in vitro* and *in vivo*.

DOI: 10.1103/PhysRevE.76.016103 PACS number(s): 82.20.Wt, 81.16.Dn, 82.35.Pq

I. INTRODUCTION

Biological systems illustrate many of the challenges in understanding molecular self-assembly far from equilibrium. The dynamics of these systems span a hierarchy of time and length scales, and the local interactions are often anisotropic. For example, understanding cytoskeletal structures formed from filaments of actin and its cross-linkers requires one to account for both asymmetric protein-protein interactions and filament flexibility at the same time as polymerization and reorganization of the filament network. Models that treat the molecular species explicitly have these features [1], but such approaches are generally too numerically demanding at present to permit statistically meaningful characterization of the dynamics.

Simplified models not only offer computational advantages but can also clarify the essential physics of such systems. Most previous studies of filament growth at the leading edge of a cell build on the polymerization ratchet picture [2–4]. The essential idea is that thermal fluctuations in filaments allow actin monomers to insert at barbed ends close to the membrane and then rectification drives protrusion. Mean-field treatments of such models show that they can account for the exponential dependence of velocity on the load observed for microtubules [5]. This result is supported by explicit simulations of filaments interacting with obstacles [6].

In comparison with the force-velocity relationship, little is known about how different actin binding proteins promote observed cytoskeletal morphologies. One simulation indicated that the number of branches per filament in solutions of polymerizing actin exhibits a maximum at a finite concentration of the branching factor actin-related protein 2/3 (Arp2/3) due to actin monomer depletion effects [7]. However, the position of branching was unrestricted in that case, and more recent theoretical work suggests that spatial control of Arp2/3 activation is important for obtaining cytoskeletal morphologies like those observed at the leading edges of cells [8]. There are even fewer studies of bundling than branching. They have largely been limited to general theories for the phase behavior of cross-linked rods in solution [9–11], but there are also a few studies of how existing bundling interactions propagate along filaments [12–14].

In the present study, we introduce an alternative simulation approach for treating molecular self-assembly that enables for the first time the growth of competing cytoskeletal morphologies stabilized by different cross-linkers. Motivated by models for glasses [15,16], we represent the basic building blocks by a lattice of discrete variables (spins). Molecular interactions enter through pairwise terms in the energy function, and the dynamics are encoded through a set of rules (allowed transitions in a Monte Carlo procedure) based on empirical data. We apply our method to the study of an *in vitro* system in which filopodialike structures (parallel bundles of actin filaments emerging from a dendritic network) are reconstituted [17]. The model reproduces the observed morphologies as the parameters are varied to represent changes in protein concentrations. Analysis of the dynamics shows explicitly that the observed bundles derive almost exclusively from patterns of spins resembling structures speculated to be nuclei for bundles based on images of *in vitro* and *in vivo* systems [17,18]. Variation of the rate of ratcheting the surface that catalyzes branching reveals that a key feature of the system is the spatial restriction of branching. Possible extensions are discussed.

II. METHODS

Here, we describe the model and its dynamics in general form. The key features are directed interactions and restricted pathways for growth. To access times pertinent to typical self-assembly problems, we effectively integrate over molecular fluctuations by representing the system through a set of discrete variables (Potts-like spins) on a lattice. In the

*Electronic address: dinner@uchicago.edu

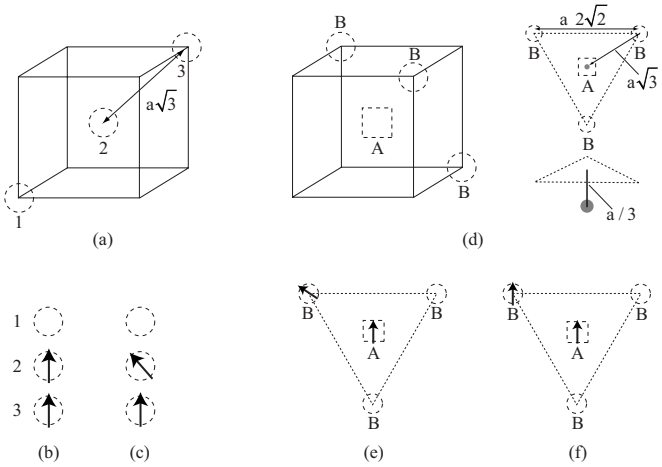

FIG. 1. Protein-protein interactions (spin-spin bonds). (a) Three sites in a linear geometry on the bcc lattice. (b) and (c) Linear and bent intrafilament spin configurations with energy contributions of $\varepsilon_{\mathrm{lin}}$ and $\varepsilon_{\mathrm{bent}}$, respectively. The dashed circles correspond to the geometry shown in (a). (d) Four sites in a nonlinear geometry on the bcc lattice. (e) and (f) Branching and bundling interfilament spin configurations with energy contributions of $\varepsilon_{\mathrm{br}}$ and $\varepsilon_{\mathrm{bu}}$, respectively. The dashed circles and square correspond to the geometry shown in (d).

cytoskeletal application that we consider in Sec. III, we restrict the system to a body-centered cubic (bcc) lattice, and the discrete variable (s_i) at each site (i) can take integer values from zero to eight. Lattice sites with $s_i=0$ correspond to regions of space with an insignificant number of monomers. The remaining values correspond to the eight possible directions on a bcc lattice. In other words, each nonzero spin points to one of its nearest-neighbor positions. The model can readily be extended to other lattice geometries; indeed, we initially implemented the model for a two-dimensional square lattice (data not shown).

Monomer-monomer and monomer–cross-linker interactions enter through pairwise terms in the energy function, and the dynamics are encoded through a set of rules analogous to facilitation constraints in models of glasses [15,16]. The system energy is a sum over nearest-neighbor pairs (denoted by $\langle ij\rangle$):

$$E=\frac{1}{2}\sum_{\langle ij\rangle}\left[E_{\mathrm{lin}}(i,j)+E_{\mathrm{bent}}(i,j)+E_{\mathrm{br}}(i,j)+E_{\mathrm{bu}}(i,j)\right], \quad (1)$$

where $E_{\mathrm{lin}}(i,j)$, $E_{\mathrm{bent}}(i,j)$, $E_{\mathrm{br}}(i,j)$, and $E_{\mathrm{bu}}(i,j)$ correspond to linear and bent intrafilament, branching, and bundling interactions between sites i and j (Fig. 1). Each of these terms is equal to a constant when the spins at sites i and j are in an appropriate geometry (detailed below) and zero otherwise.

The spin system does not have intrinsic dynamics. We assume Markovian behavior and employ a kinetic Monte Carlo procedure to simulate the dynamics of the model (Appendix A). To restrict kinetic pathways to ones consistent with biochemical and structural data, the rate of changing a spin at each step depends on the local geometry. Specifically, the rate for a transition of type p (in our case, either growth, denoted g, or branching, denoted b, shown in Fig. 2) that changes the spin value at site i from s_i to s_i' with the configuration of the remaining spins $(j\neq i)$ denoted μ is

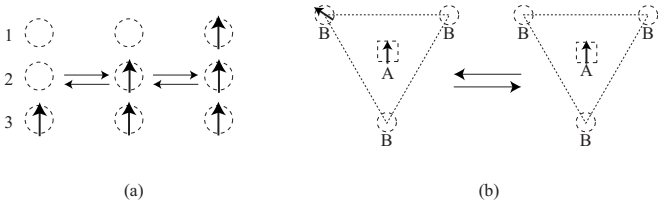

FIG. 2. Allowed moves of the kinetic Monte Carlo dynamics [transitions of type p in Eq. (2)]. (a) Growth and relaxation $(p=g)$: facilitated spins can take any value. The geometry of the dashed circles is that in Fig. 1(a). (b) Branching $(p=b)$: only the indicated spin values are possible (see Sec. III A 2). The geometry of the dashed circles and squares is that in Fig. 1(d).

$$w(s_i\to s_i'|\mu)=k_p\Theta_p(s_i\to s_i'|\mu)\times\left(\frac{\exp\{-[E(s_i'|\mu)-E(s_i|\mu)]\}}{\sum_{s_i''}\exp\{-[E(s_i''|\mu)-E(s_i|\mu)]\}}\right). \quad (2)$$

The constant k_p is the rate constant for a transition of type p, and the function $\Theta_p(s_i\to s_i'|\mu)$ represents a constraint that imposes cytoskeletal-like dynamics by restricting the pathways of relaxation. $\Theta_p(s_i\to s_i'|\mu)=\Theta_p(s_i'\to s_i|\mu)$ is 1 for appropriate local spin geometries (illustrated in Sec. III A) and zero otherwise.

The term in large parentheses is the standard Glauber acceptance criterion [19]. We use this form over the commonly employed Metropolis one [20] because we are interested in dynamics. To understand this choice, consider a system in configuration ν that can transition to either state ν' or ν'' with energies $E(\nu)>E(\nu')>E(\nu'')$. In a Metropolis Monte Carlo simulation, the transition probabilities of both $\nu\to\nu'$ and $\nu\to\nu''$ are 1, because both moves result in a decrease in energy. In an equilibrium simulation, subsequent transitions that increase the energy $(\nu'\to\nu$ and $\nu''\to\nu)$ ensure that the states ν' and ν'' are properly weighted, but, in a nonequilibrium simulation, the system typically relaxes only further downhill in energy. The Glauber criterion weights states according to their Boltzmann probabilities in both moves that decrease the system energy and those that increase it. The Monte Carlo procedure maintains detailed balance for elementary processes (such as filament growth, relaxation, branching, and bundling). However, it is important to stress that our goal is to study the evolution of the system from nonequilibrium conditions given the Monte Carlo dynamics, not to calculate equilibrium averages.

III. APPLICATION

Filopodia are relatively long, thin membrane protrusions at the leading edge of a cell and are believed to be important for directed migration [21]. These structures are supported by bundles of parallel actin filaments rooted in the dendritic network close to the leading edge. The morphologies of

filopodia and the dendritic network from which they grow are associated with different actin crosslinking proteins. Filopodia are rich in fascin [18], a 55 kDa protein that binds parallel actin filaments [22]. The dendritic network contains abundant Arp2/3, which is known to nucleate branches on existing filaments at an angle of 70° on average [23–25]. Despite biochemical [26–29] and structural [30] characterization of these molecules, the mechanisms by which filopodia form are still poorly understood. In particular, there is a need for studies that probe the collective dynamics of actin filaments and their cross-linking proteins.

To this end, Borisy and co-workers recently studied a system [17] comprised of actin, fascin, Arp2/3, and beads coated with Wiskott-Aldrich syndrome protein (WASP), which activates Arp2/3 [31]. Depending on whether fascin was present or absent, different structures were observed. When fascin was absent, clouds of dendritic structure surrounded the beads; when fascin was present, bundles radiated outward from a dendritic halo. There was no growth of any kind without Arp2/3. This system provides a means of reconstituting filopodialike bundles rooted in a dendritic network *in vitro*. However, the role of Arp2/3 in bundle formation is not clear. Borisy and co-workers suggest that densities of barbed ends comparable to those found in dendritic networks are necessary for filaments to intersect and initiate bundles. Static electron micrographs of *in vivo* systems show precursors resembling the Greek letter Λ [18], but it is not experimentally possible to identify the critical events that lead to their formation. Models can thus play an important role in interpreting these data.

A. Representations of elementary processes

To define the energy and constraint functions for the model [Eqs. (1) and (2)], it is necessary to ask what are the essential physical processes operating in the system of interest. Answering this question at a level that permits formulation of the model is in itself highly informative. In the *in vitro* experiments described above [17], filaments must grow, branch in the presence of Arp2/3, and bundle in parallel in the presence of fascin. An additional feature that is less obvious is that, for branching to occur at significant rates, a catalyst, such as WASP or a protein related to it like Scar or ActA, is required [31]. The experiments of interest use beads coated with WASP, which restricts branching to regions close to their surfaces [17]. Below, we describe the minimal set of energy and constraint functions that captures the key dynamics.

1. Filament growth and relaxation

Filaments change length primarily by actin polymerization and depolymerization at their barbed and pointed ends. We only consider growth at the barbed end, which is rapid compared with that at the pointed end (11.6 and 1.3 $\mu M^{-1}\,s^{-1}$, respectively [32]). We neglect spontaneous filament nucleation because fits of polymerization data suggest that actin dimers and trimers depolymerize $\sim 10^4$ times faster when not associated with Arp2/3 [23]. Similarly, we neglect filament aging due to ATP hydrolysis because it is much slower than the other processes considered (Pollard *et al.* [28] estimated rates between 0.02 and 0.10 s^{-1}).

The E_{lin} term contributes a favorable energy ($\varepsilon_{\mathrm{lin}}<0$) for each pair of parallel spins in sequence [Fig. 1(a)]. The E_{bent} term contributes a smaller but still favorable energy ($\varepsilon_{\mathrm{bent}}<0$) for each pair of spins that make a 70.5° angle, the smallest nonlinear angle on the bcc lattice in which one spin points at the other [Fig. 1(b)]. In the model, sites with nonzero spins facilitate transitions at the sites to which they point; a site to which a nonzero spin points can take any value (zero through eight). In Eq. (2), $\Theta_g(s_i \rightarrow s_i' \,|\, \mu)=1$ for all s_i and s_i' at the sites marked by circles in Fig. 2(a), and $\Theta_g(s_i \rightarrow s_i' \,|\, \mu)=0$ otherwise. In using a constant rate for growth-type transitions (k_g), we assume that the monomer concentration in solution is sufficiently homogeneous that the rate of polymerization is directly proportional to the number of barbed ends. However, it is important to note that, in addition to allowing growth at barbed ends, such moves permit the system to relax to some extent because each spin along a filament points to the next; $\varepsilon_{\mathrm{lin}}$ and $\varepsilon_{\mathrm{bent}}$ are chosen such this mechanism does not lead to filaments with an excessive number of defects.

2. Branching

The protein Arp2/3 binds actin and nucleates branches with free barbed ends that make a 70° angle with the parent filament in the presence of a catalyst [23–25,33,34]. We represent the WASP-coated bead by allowing branching moves [Fig. 2(b) and described immediately below] only within a distance d_{br} of one face of the lattice. Approximating the curved surface by a flat one is reasonable given that the radius of the beads used by [17] is 0.5 μm compared with 3 nm for an actin filament [32], and we restrict our attention to early events in bundle formation.

For the unit vector $\mathbf{s}_i$ in the direction corresponding to spin value s_i at site i and the unit vector $\mathbf{d}_{ij}$ in the direction of the vector from site i to site j, branching can be facilitated at site j when $\mathbf{s}_i \cdot \mathbf{d}_{ij}=1/\sqrt{3}$. The spin at site j can transition between values 0 and that corresponding to $\mathbf{d}_{ij}$ [Fig. 2(b)]. If the site contains a spin value inconsistent with these criteria, branching at j cannot be facilitated by site i even though it can still be facilitated by another site. Regardless of their history, branchlike geometries [Fig. 1(c)] are stabilized once formed by the $E_{\mathrm{br}}(s_i, s_j)$ term in Eq. (1).

3. Bundling

Recent FRAP measurements of fascin *in vivo* suggest that fascin dynamics are fast, with a fluorescence recovery half-life of less than 10 s [35]. We thus assume that fascin quickly reaches a quasiequilibrium between bound and unbound states when filaments are at the right separation and orientation for cross-linking. Due to this simplification, bundling enters the model only through the energy function [Eq. (1)] rather than the transition rates used for branching and filament growth [Eq. (2)]. A contribution of $\varepsilon_{\mathrm{bu}}$ is added to the energy for each pair of spins that are noncollinear, adjacent, and parallel [Fig. 1(d)].

TABLE I. Parameters varied to represent changes in protein concentrations and summary of consequent morphologies. Energies are in dimensionless units, and the rate constants are in units of inverse dimensionless time $1/\tau_{sim}$.

Regime	ε_{lin}	ε_{bent}	k_{br}	k_{surf}	ε_{bu}	Observed behavior
A^-F^-	−10	−2	0.0	Any	−4	Virtually no growth
A^+F^-	−10	−2	0.1	0	0	No bundles, filaments face away from surface
A^+F^+	−10	−2	0.1	0	−4	Bundles, filaments face away from surface
$A^+F^-S^+$	−10	−2	0.1	0.0005	0	No bundles, filaments face surface
$A^+F^+S^+$	−10	−2	0.1	0.0005	−4	Bundles, filaments face surface

4. Surface ratcheting

A common feature of theoretical studies of the cytoskeleton is growth against an obstacle (for example, see [6]). Indeed, in the *in vitro* experiment, the fact that dendritic structure is observed far from the WASP-coated bead implies that beads and filament networks move relative to each other as the system grows, presumably due to Brownian ratchet forces [2,36]. In our simulation, we represent this feature by moving the surface that represents the WASP-coated bead away from the existing spins with a rate proportional to the spins within one lattice site of it, independent of their orientation. In such a move, the surface advances a number of lattice sites chosen at random from a uniform distribution in the interval $[1, d_{surf}]$. Although the majority of our local moves maintain microscopic reversibility, surface diffusion does not.

B. Choice of parameters

To the greatest extent possible, parameter values (Table I) were chosen based on available data. The simulation has four energy parameters: ε_{lin}, ε_{bent}, ε_{br}, and ε_{bu}. The energies ε_{lin} and ε_{bent} were varied to obtain a persistence length of $\sim 10^3$ lattice units for a single filament, which we take to be the persistence length of actin, 15 μm [32]. This choice corresponds to 15 nm per bcc lattice bond ($a\sqrt{3}$), which is roughly twice the diameter of an actin filament [32]. Due to the coarse-grained nature of the model, in which complex protein-protein interactions are reduced to pairwise spin terms, it is not possible to estimate ε_{br} and ε_{bu} directly. Instead, we explored a wide range of values to identify parameter regimes that yielded reasonable morphologies, and found that the results depended primarily on the relative size of the branching and bundling terms. In our model, branches can arise from facilitated "growth" as well as the branching move; to minimize the contribution from this alternate pathway, $|\varepsilon_{bu}| > |\varepsilon_{bent}| \geqslant |\varepsilon_{br}|$ is required.

The simulation has three rate parameters: k_g, k_{br}, and k_{surf}. We use the inverse of the first of these to define a dimensionless unit of time ($\tau_{sim} \equiv 1/k_g$) and express the other two rates in terms of it. At concentrations of 10–100 μM, actin filaments elongate at a rate of 0.3–3 μm/s in dilute buffers [28]. In the experiments of interest [17], the actin concentration is 6.9 μM. We thus assume that polymerization takes place at 0.1 μm/s, which corresponds to 7 lattice sites/s. Given that k_g sets the unit of simulation time (τ_{sim}) at about 0.1 s, the simulations ($500\tau_{sim}$) correspond to experimental observation periods of about 1 min.

The remaining rate parameters k_{br} and k_{surf} cannot be set independently because they model composite processes (binding of Arp2/3 to WASP, filament extension, and thermal ratcheting). Branching was allowed at sites either on the surface or $a = 1/\sqrt{3}$ away from it (the point-to-plane distance of the nearest neighbors of sites lying in the surface). Given this restriction, we explored a range of values for k_{br} and k_{surf} (Table II). We found that higher rates of branching primarily created higher densities of spins on the lattice with few other qualitative features. We chose the value $k_{br} = 0.1/\tau_{sim}$ because it generated a density of spins that was sufficiently high to allow substantial bundle formation but low enough that the lattice did not saturate with spins, and cytoskeletal-like structures could be observed. For this choice of parameters, the surface moved steadily for $k_{surf} > 10^{-4}/\tau_{sim}$ and its average speed saturated in a k_{br}-dependent manner due to the fact that creation of new spins adjacent to the surface eventually becomes limiting.

The lattice was $150 \times 150 \times 400$ in the Cartesian directions (but, as discussed in [37], 3/4 of the sites are unused). Simulations began with 100 seed spins pointing at the surface and 5–15 lattice units ($a = 1/\sqrt{3}$) from it. We assume that growth around the bead eventually reduces its thermal motion and thus limit the number of ratcheting moves in the simulation. Specifically, the surface was allowed to move a distance of 50 units in Cartesian directions ($50 \times 1/\sqrt{3}$ lattice units, or 0.75 μm).

The diffusion constant for free actin monomers has been measured to be between 49 and 61 $\mu m^2/s$ in buffer [38] and between 4.6 and 7.0 $\mu m^2/s$ *in vivo* [39]. Using a conserva-

TABLE II. Average speeds of the surface (lattice units/τ_{sim}) for different choices of the branching and surface ratcheting rate constants. The rate constants for branching (k_{br}) and surface ratcheting (k_{surf}) are in units of inverse dimensionless time, $1/\tau_{sim}$.

	k_{br}	
k_{surf}	0.1	0.5
10^{-4}	0.048	0.286
10^{-3}	0.260	0.533
10^{-2}	0.537	0.754
10^{-1}	0.555	0.866

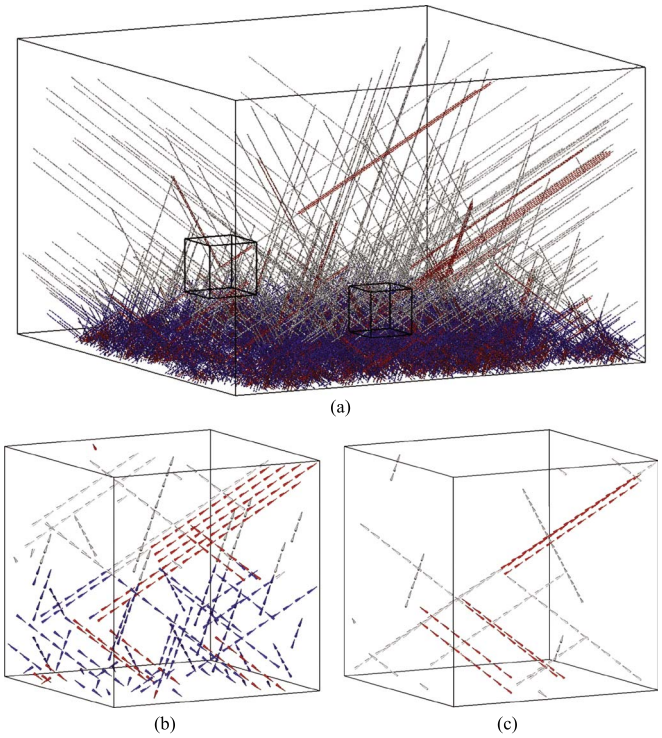

FIG. 3. (Color online) Representations of a snapshot of an A^+F^+ simulation at time $250\tau_{\mathrm{sim}}$. (a) Snapshot showing filaments (silver), bundled filaments (red), and dendritic structure near the surface (blue). (b) Region identified by the lower right box in (a), which shows the structures associated with bundle nucleation at the edge of the dendritic region. (c) Region identified by the upper left box in (a), which shows the structures associated with bundle nucleation away from the dendritic region.

tive value of 4.5 $\mu\mathrm{m}^2/\mathrm{s}$, a monomer would take about 0.1 s to travel across the simulation box. Because we create spins at a rate of 10 spins/s and each nonzero spin accounts for roughly six monomers based on the size of the unit cell, it is in principle possible that monomers would become locally depleted close to the surface where growth is fastest. In the present simulations, we neglect this scenario. The model could be extended to include it by making k_g and k_{br} depend on the local spin density.

C. Observation of dendritic and bundled morphologies

Protein concentrations enter the model through the choice of parameters in Eqs. (1) and (2) (Table I). The concentration of Arp2/3 is modulated by the rate of branching at the surface (k_{br}). In contrast to Arp2/3, we assume that fascin binds and unbinds rapidly when filaments are appropriately aligned, as suggested by [35]. The concentration of fascin is thus modulated by the pairwise interaction energy associated with parallel spins ($\varepsilon_{\mathrm{bu}}$); in particular, we consider fascin to be absent when $\varepsilon_{\mathrm{bu}}=0$. We see no significant growth when Arp2/3 is absent ($k_{\mathrm{br}}=0.0$, denoted A^-F^-). When Arp2/3 but not fascin is present ($k_{\mathrm{br}}=0.1$ and $\varepsilon_{\mathrm{bu}}=0$, denoted A^+F^-), dendritic structure forms close to the face of the lattice which represents the bead surface (Fig. 3). When both Arp2/3 and fascin are present ($k_{\mathrm{br}}=0.1$ and $\varepsilon_{\mathrm{bu}}=-4$, denoted A^+F^+), parallel bundles of spins emerge from the dendritic structure. Thus the model captures the three major morphologies observed by Vignjevic *et al.* [17].

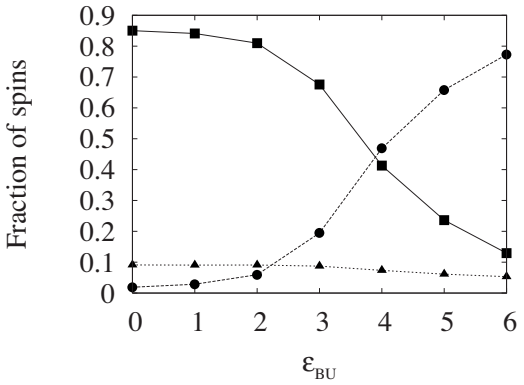

FIG. 4. Fraction of spins with patterns of interactions characteristic of bundles. The solid line with square symbols shows the fraction of spins with only linear interactions [Fig. 1(a)]. The dashed line with circular symbols shows the spins with both bundling and linear interactions [Fig. 1(d)]. The dotted line with triangular symbols shows the fraction of spins with branch interactions. Data are for snapshots corresponding to $t\approx 350\tau_{\mathrm{sim}}$.

To characterize the three parameter regimes statistically, we examined distributions of spins and their interactions. We calculated the fractions of spins having only linear interactions and spins having both linear and bundling (but no other) interactions for selected time points in simulations with different pairwise bundling energies (Fig. 4). Consistent with the examples shown in Fig. 3, the amount of bundling increases significantly with $|\varepsilon_{\mathrm{bu}}|$; this trend is mirrored by a loss of spins not participating in cross-linking interactions (Fig. 4). The two fractions of spins do not account for the small number of spins with branching ($\varepsilon_{\mathrm{br}}$) or bent ($\varepsilon_{\mathrm{p2}}$) interactions. To verify that the increase in the fraction of spins with both linear and bundling interactions was indeed due to an increase in structures that corresponded to visually apparent bundles, we identified groups of contiguous spins with bundling interactions by tracing their connectivity with a breadth-first search algorithm. These structures had much wider cross sections (cuts orthogonal to the spin direction) in the A^+F^+ case than the A^+F^- one [Fig. 5(a)]. The distribution of lengths for the wider structures ($\langle\mathrm{width}\rangle\geqslant 4$) is shown for the A^+F^+ case in Fig. 5(b), and confirms that they do indeed correspond to bundlelike patterns of spins.

D. Characterization of nuclei

Vignjevic *et al.* [17] propose two mechanisms for *in vitro* bundle formation and growth. Smaller bundles are thought to derive from filament intersections similar to Λ precursors observed *in vivo* [18], while larger ones are formed by zippering of existing structures. Because our simulations are limited to relatively short times and the lattice precludes large-scale collective motions, we focus on the former mechanism. To this end, we defined two patterns of spins that resemble Λ precursors (Fig. 6) and counted the number of bundles that grew from them with the algorithm described

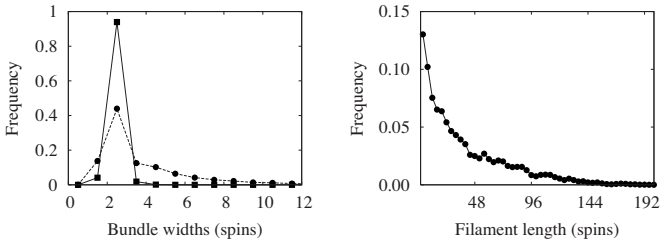

FIG. 5. (a) Probability distribution of bundle widths for the A^+F^+ (dashed line, circular symbols) and A^+F^- (solid line, square symbols) parameter sets. To determine bundle widths, we count sequences of parallel spins connected by bundling interactions [Fig. 1(d)], restricted to a narrow distance orthogonal to the plane determined by each spin vector. We divide the lattice into strips of narrow thickness and count the number of bundling spins contained entirely within a strip. Here a strip around site i is defined by all sites j whose distance vector with site i, $\mathbf{d}_{ij}$ satisfy the relation for a strip at site i $|\mathbf{s}_i \cdot \mathbf{d}_{ij}| \leq 1/\sqrt{3}$. (b) Lengths of bundles with widths greater than four spins in the A^+F^+ case. Both the width and length distributions were computed over the entire lattice.

in Appendix B. Although at very early times most bundling interactions result from chance parallel spin pairings, by the end of the simulations, on average more than 80% of the bundled spins derived from the Λ-precursor-like patterns of spins (Fig. 7); types I and II were roughly equally represented. As evidenced by the initial phase of the simulation, the Λ-precursor mechanism need not have been the predominant one for bundle formation in the model, so we believe that this observation is significant.

Λ-precursor-like patterns of spins formed at rates independent of the lattice configuration once filaments reached the surface and began branching ($t \approx 50\tau_{\mathrm{sim}}$). The rate for forming type I nuclei *de novo* was $3.16/\tau_{\mathrm{sim}}$ and that for forming type II nuclei was $10.22/\tau_{\mathrm{sim}}$ for $t < 200\tau_{\mathrm{sim}}$ and $6.37/\tau_{\mathrm{sim}}$ for $t > 200\tau_{\mathrm{sim}}$. These statistics were obtained from linear fits with Pearson linear correlation coefficients of $r^2 > 0.95$. Interconversion between the two types was well described by kinetics that were first order in the numbers of

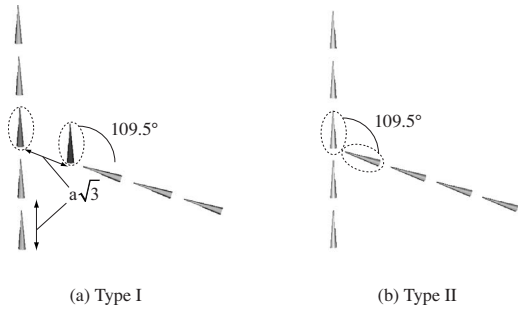

FIG. 6. Schematic evolution of bundles formed by Λ-precursor-like routes. Bundles are formed through the type I intermediate, which either can be spontaneously generated on the lattice, or can result from a type II configuration converting to a type I configuration. (a) Type I configurations: the circled spins share an $\varepsilon_{\mathrm{bu}}$ bond. (b) Type II configurations: the circled spins share an $\varepsilon_{\mathrm{bent}}$ bond.

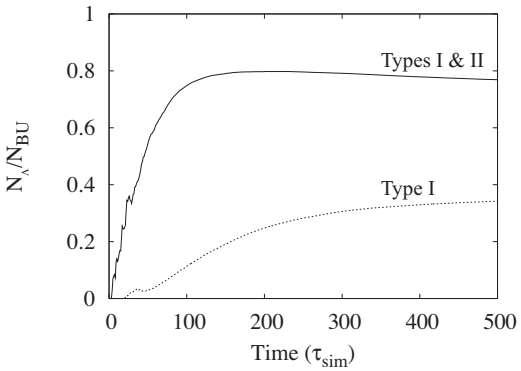

FIG. 7. Time evolution of bundled spins that originate from Λ-precursor-like patterns of spins. Labels correspond to the spin patterns in Fig. 6. Results are averages over ten simulations of $500\tau_{\mathrm{sim}}$ length with sampling at approximately $1\tau_{\mathrm{sim}}$ intervals. These data were generated without surface ratcheting ($k_{\mathrm{surf}}=0/\tau_{\mathrm{sim}}$), but virtually identical results were obtained at $k_{\mathrm{surf}}=0.0005/\tau_{\mathrm{sim}}$.

Λ-precursor-like patterns of spins (based on linear fits with $r^2 \geq 0.90$). Type I patterns interconverted to type II patterns with rate 0.0286 per type I pattern; type II patterns interconverted to type I patterns with rate 0.0168 per type II pattern. Comparison of these data with the fact that observed bundles derive from both structures with roughly equal likelihoods suggests that type II spin patterns form frequently and then slowly convert to type I spin patterns before they can initiate a bundle, while type I spin patterns form infrequently but then initiate bundles rapidly. In the experimental system, these dynamics correspond to fluctuations in position of the tip of a filament required to capture a fascin molecule for bundling. In this regard, it is worth noting that in contrast to the cartoon in Vignjevic *et al.* [[17], Fig. 8], bundles predominantly (greater than 65% of events) formed from the collision of a tip with an existing filament, not collisions betweeen two tips.

E. Number and orientation of bundles depend on surface ratcheting

To validate the model and the microscopic insights gained from it, we explore its behavior while varying its experimentally manipulable parameters. To this end, we focus on the rate constant for surface ratcheting (k_{surf}) which is qualitatively related to the resistance to movement of the beads in the experiment [17]. This resistance can be controlled through the viscosity of the medium or the shape and size of the bead. We characterize the behavior by counting bundles, which again we identify as groups of spins connected by linear and bundling interactions.

The total number of bundles varies nonmonotonically with k_{surf} and exhibits a maximum at $k_{\mathrm{surf}} \approx 0.0002/\tau_{\mathrm{sim}}$ (Fig. 8). In these simulations, we allowed the surface to move 200 units in Cartesian directions (3.0 μm) to account for greater surface movement at larger k_{surf}. At low k_{surf}, which corresponds to a regime of large viscous drag, the surface is essentially stalled, and most of the bundles are oriented away

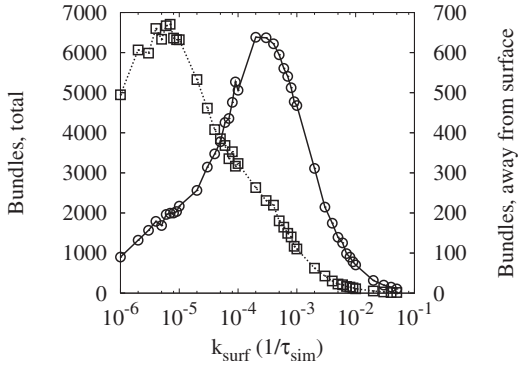

FIG. 8. Numbers of bundles as a function the rate of surface ratcheting. The solid line with circular symbols and left scale correspond to all bundles; the dashed line with square symbols and right scale are restricted to bundles oriented away from the surface. Results are averages over ten simulations with $k_{br}=0.1/\tau_{sim}$ and $\varepsilon_{bu}=-4$; $t\approx 250\tau_{sim}$.

from the surface, as in the cases in [17] on which we have concentrated. As the rate of surface ratcheting increases (the viscous drag decreases), the surface moves at a steady speed, and most of the bundles become oriented toward the surface, which corresponds experimentally to the case that a comet-like tail is formed [17,40]. At very high k_{surf}, an experimentally inaccessible regime is reached in which the surface moves too quickly for Arp2/3 to nucleate branches, and the density of filaments becomes too low for bundles to nucleate.

To understand these results in detail, it is important to appreciate that the number of bundles oriented away from the surface is correlated with the number of branch sites with spins pointed away from the surface ($r^2=0.89$). Each spin close to the surface can facilitate branching at three sites (Sec. III A 2). Of these three sites, only one corresponds to a secondary spin directed away from the surface when the primary spin is pointed towards the surface. As the rate of surface ratcheting increases, the average time a spin stays adjacent to the surface decreases. As a result, at higher k_{surf}, there is less opportunity to generate both new spins in general (which decreases the overall density and thus the chance of filament-tip collisions) and ones pointed away from the surface (which decreases the number of bundles oriented away from the surface). By the same token, the nonmonotonic trend in the total number of bundles comes from the fact that the overall density decreases with k_{surf} but the ability to elongate, once formed, increases with it.

IV. DISCUSSION

In the present study, we introduced a coarse-grained computational approach for treating self-assembly and applied it to actin filament growth and cross-linking. Directed interactions and restricted pathways for growth enable treatment of self-assembly of anisotropic elements; the fact that small fluctuations are "preaveraged" allows much greater statistical characterization of the parameter space than do off-lattice simulations that maintain greater chemical detail [1]. The method is in the spirit of cellular automata [41] and, more generally, agent-based approaches [42], which have been applied to self-organization in other contexts (see also [43]). An important distinction is that elementary processes in our model are microscopically reversible, reflecting their thermally activated origin. Indeed, the process of selecting energy and constraint functions that satisfy this requirement and capture the essential dynamics of a system provides insight in itself. The elementary processes that we consider are filament growth, branching, and parallel bundling.

The one process that we include that does not obey detailed balance is the movement of the surface that represents the WASP-coated bead that catalyzes Arp2/3 incorporation for barbed end generation in the *in vitro* system of interest [17]. This difference from the other elementary processes reflects the fact that, physically, the movement is driven by a polymerization ratchet [2–4]. The rate of surface ratcheting, which is qualitatively related to the viscous drag on the beads in the experiments, was found to control whether bundles formed such that they were oriented towards or away from the surface. These simulations, along with ones in which d_{surf} was made infinite (data not shown), reveal the importance of the spatial restriction of branching for obtaining distinguishable dendritic and bundled regions in our lattice model.

Extending the model to include other cytoskeletal processes (such as filament severing, capping, and antiparallel bundling) should be straightforward. More challenging will be the incorporation of an elastic membrane, which is expected to be important for studying protrusive and lateral growth of bundles *in vivo* [12,13] as well as filament orientation in dendritic networks [44]. As the model stands, the local nature of the Monte Carlo moves and the orientational restrictions associated with the discrete nature of the lattice do not enable large-scale collective motions such as zippering to occur readily. Nevertheless, to the best of our knowledge, the present work is the first theoretical contribution that explicitly demonstrates a mechanism for how bundles are nucleated within a branched dendritic network of actin filaments. We thus believe the approach warrants further consideration for modeling molecular self-assembly.

ACKNOWLEDGMENTS

The authors wish to thank Tobin Sosnick and Tom Witten for critical readings of the manuscript.

APPENDIX A: MONTE CARLO PROCEDURE

Here, we describe how the rates for different processes are used to determine the moves performed, followed by implementation details.

1. Algorithm

The algorithm that we employ to simulate filament dynamics is a variant of the original Bortz-Kalos-Lebowitz continuous-time Monte Carlo algorithm [45] but is cast in the formulation presented by Gillespie for chemical systems [46]. Following Gillespie [46], we write the transition between lattice states in terms of rate laws. The current lattice

configuration is μ, and the set of all lattice configurations that can be reached from the current configuration is $\{\nu: \nu \neq \mu\}$. Typically $\mu \rightarrow \nu$ corresponds to changing the value of a single spin. The differential changes associated with exiting the current configuration μ and entering the new configuration ν are, respectively,

$$dP_\mu = -\left(\sum_{\nu \neq \mu} W(\mu \rightarrow \nu)\right) P_\mu dt = -W_\mu^{\mathrm{tot}} P_\mu dt, \quad \text{(A1)}$$

$$dP_\nu = W(\mu \rightarrow \nu) P_\mu dt. \quad \text{(A2)}$$

$W(\mu \rightarrow \nu)$ is a sum over all elementary rates w [Eq. (2)] that take the lattice from configuration μ to ν. In particular, for a single spin flip $(s_i \rightarrow s_i')$, $W(\mu \rightarrow \nu) = w(s_i \rightarrow s_i' | \mu)$ [Eq. (2)]. Because the transition between two configurations is constant at each step, each configuration μ has a constant total rate of exit [W_μ^{tot}, defined by Eq. (A1)] and the probability of staying in the current configuration μ until time t is obtained by integrating Eq. (A1) to obtain

$$P_\mu(t < \Delta t) = \exp(-W_\mu^{\mathrm{tot}} \Delta t). \quad \text{(A3)}$$

As a result, the time to leave the current configuration μ is calculated according to

$$\Delta t = -\ln(a_0)/W_\mu^{\mathrm{tot}}, \quad \text{(A4)}$$

where a_0 is a random number chosen uniformly from the interval [0, 1) [47]. By the same token, the probability of entering a new state ν is obtained by substituting P_μ into Eq. (A2) and integrating; the result is

$$P_\nu(t < \Delta t) = W(\mu \rightarrow \nu)[1 - \exp(-W_\mu^{\mathrm{tot}} \Delta t)]/W_\mu^{\mathrm{tot}}. \quad \text{(A5)}$$

The probability of the transition $\mu \rightarrow \nu$ relative to $\mu \rightarrow \nu'$ is then $P_\nu(t)/P_{\nu'}(t) = W(\mu \rightarrow \nu)/W(\mu \rightarrow \nu')$. Indexing the possible transitions by m ($\{\mu \rightarrow \nu_m\}$), we choose state ν_n such that

$$\sum_{m=1}^{n-1} W(\mu \rightarrow \nu_m) \leq a_1 W_\mu^{\mathrm{tot}} < \sum_{m=1}^{n} W(\mu \rightarrow \nu_m), \quad \text{(A6)}$$

where a_1 is another uniformly distributed random number in [0, 1). Equations (A4) and (A6) form the heart of an algorithm that weights fast and slow processes correctly in an efficient fashion (see [48] for further discussion of continuous-time algorithms).

2. Implementation details

In our algorithm [Eqs. (A4) and (A6)], the number of possible moves grows with the number of nonzero spins on the lattice. Choosing the time step and move from a list scales linearly with N moves, or $O(N)$. As in several recent studies [37,48–50], we use a binary tree structure to reduce the scaling to $O(\log N)$.

Each node in the tree holds five values: (1) the lattice site index i, (2) the new spin s_i', (3) the rate at which the site, in the current lattice configuration μ, will change to the new spin $\kappa_{\mathrm{move}} = w(s_i \rightarrow s_i' | \mu)$, (4) the total rate of exit to all nodes of this branch of the tree, including that of the node, κ_{branch}, and (5) the left (L) and right (R) children of the node. We aggregate rates from all moves with the same (site, spin) pair and store only the total rate at which the site will transition to that spin. In other words, there is a one-to-one relation between nodes in the tree and site-spin pairs. The children (branches) of a node are ordered $L < (\text{parent}) < R$ by defining the inequality $(i, s_i) < (j, s_j)$ if and only if $i < j$ or $i = j$ and $s_i < s_j$. The root of the tree always holds the sum of all rates (W_μ^{tot}) in its κ_{branch} value.

Given a_1 [Eq. (A6)], we determine the next state by performing a binary search of the tree, which is sorted by (site, new spin value) pair:

(1) Start with N at the root of the tree; L is the left child of N, and R is the right child of N. Set $\kappa_{\mathrm{curr}} = W_\mu^{\mathrm{tot}} a_1$.

(2) If $\kappa_{\mathrm{curr}} \leq \kappa_{\mathrm{branch}}(L)$ then set N to be L (the left child) and update L and R accordingly; repeat this step. Otherwise, $\kappa_{\mathrm{curr}} = \kappa_{\mathrm{curr}} - \kappa_{\mathrm{branch}}(L)$.

(3) If $\kappa_{\mathrm{curr}} \leq \kappa_{\mathrm{move}}(N)$, return N as the selected move. Otherwise, $\kappa_{\mathrm{curr}} = \kappa_{\mathrm{curr}} - \kappa_{\mathrm{move}}$.

(4) Descend to the right child; set N to be R and update L and R accordingly. Go to step 2.

Once a move is chosen and the lattice is updated, we determine the new possible moves and their rates at the site chosen and those surrounding it (nearest neighbors and next-nearest neighbors for a total of nine sites). In turn, each site on the lattice can be associated with at most nine nodes in the tree, eight for new spin values and one for surface diffusion. The number of nodes affected by a nonsurface move is thus bounded by $(8+1) \times 9 = 81$. In practice, not all of the nine sites are facilitated to flip to all nine spin values, and only spins on one face of the lattice influence surface diffusion, so the actual number of nodes updated is often much smaller.

To ensure that data storage and retrieval does not compromise the gains in efficiency associated with the binary search, the tree was rebalanced with the AVL algorithm [51]. Surface ratcheting moves trigger recalculation of rates for the entire lattice, but this move is infrequent. The overall computational time thus scales as $O(\log n)$, where n is the number of nonzero spins. For the $0.25 \times 150 \times 150 \times 400 = 2250000$ accessible sites on the bcc lattice simulated, assuming 25% of these sites are occupied, a simple list implementation involves a search through $9 \times 0.25 \times 2250000 \approx 5 \times 10^6$ possible moves each step. In contrast, our implementation requires only $10 \times \log_2(5 \times 10^6) = 10 \times 22.3 \sim 10^2$ operations.

APPENDIX B: TRACKING LATTICE DYNAMICS

To investigate the dynamics of formation of Λ-precursor-like structures, we use a bookkeeping system in which spins are "colored" ("red" for bundled spins deriving from a type I nucleus, "blue" for spins in a type II nucleus, and "green" for bundled spins not derived from one of these patterns of spins). The algorithm processes snapshots of the lattice in sequence. Each snapshot is scanned three times. The first scan identifies previously uncolored spins that now

correspond to type I nuclei (red) or type II nuclei (blue). Here we examine the lattice for conversions between type I and type II nuclei, and update their colors accordingly. The second scan looks for uncolored spins that either grew from red spins or are bundled to red spins. When a red spin points to an uncolored spin, the uncolored spin is colored red. Each uncolored spin bundled to a red spin is also colored red. A depth-first search is used to identify all the spins that have grown from or bundled to a red spin. The third scan looks for uncolored, bundled spins. We then color these spins green. This color is used to avoid coloring spins red if the spins belonged to preexisting bundled structures. Each red spin then represents a spin that belongs to a bundle that formed through a Λ-precursor-like structure.

[1] J. B. Alberts and G. M. Odell, PLoS Biol. **2**, 2054 (2004).
[2] C. S. Peskin, G. M. Odell, and G. F. Oster, Biophys. J. **65**, 316 (1993).
[3] A. Mogilner and G. F. Oster, Eur. Biophys. J. **25**, 47 (1996).
[4] A. Mogilner, Curr. Opin. Cell Biol. **18**, 32 (2006).
[5] M. Dogterom and B. Yurke, Science **278**, 856 (1997).
[6] A. E. Carlsson, Phys. Rev. E **62**, 7082 (2000).
[7] A. E. Carlsson, M. A. Wear, and J. A. Cooper, Biophys. J. **86**, 1074 (2004).
[8] E. Atilgan, D. Wirtz, and S. X. Sun, Biophys. J. **89**, 3589 (2005).
[9] A. Zilman and S. A. Safran, Europhys. Lett. **63**, 139 (2003).
[10] I. Borukhov, R. F. Bruinsma, W. M. Gelbart, and A. J. Liu, Proc. Natl. Acad. Sci. U.S.A. **102**, 3673 (2005).
[11] J. Kierfeld, T. Kuhne, and R. Lipowsky, Phys. Rev. Lett. **95**, 038102 (2005).
[12] A. Mogilner and B. Y. Rubinstein, Biophys. J. **89**, 782 (2005).
[13] E. Atilgan, D. Wirtz, and S. X. Sun, Biophys. J. **90**, 65 (2006).
[14] L. Yang, D. Sept, and A. E. Carlsson, Biophys. J. **90**, 4295 (2006).
[15] G. H. Fredrickson and H. C. Andersen, Phys. Rev. Lett. **53**, 1244 (1984).
[16] J. P. Garrahan and D. Chandler, Proc. Natl. Acad. Sci. U.S.A. **100**, 9710 (2003).
[17] D. Vignjevic, D. Yarar, M. D. Welch, J. Peloquin, T. Svitkina, and G. G. Borisy, J. Cell Biol. **160**, 951 (2003).
[18] T. M. Svitkina, E. A. Bulanova, O. Y. Chaga, D. M. Vignjevic, S. Kojima, J. M. Vasiliev, and G. G. Borisy, J. Cell Biol. **160**, 409 (2003).
[19] R. J. Glauber, J. Math. Phys. **4**, 294 (1963).
[20] N. Metropolis, A. W. Rosenbluth, M. N. Rosenbluth, and A. H. Teller, J. Chem. Phys. **21**, 1087 (1953).
[21] J. V. Small, T. Stradal, E. Vignal, and K. Rottner, Trends Cell Biol. **12**, 112 (2002).
[22] S. Yamashiro-Matsumura and F. Matsumura, J. Biol. Chem. **260**, 5087 (1985).
[23] R. D. Mullins, J. A. Heuser, and T. D. Pollard, Proc. Natl. Acad. Sci. U.S.A. **95**, 6181 (1998).
[24] T. M. Svitkina and G. G. Borisy, J. Biol. Chem. **145**, 1009 (1999a).
[25] L. Blanchoin, K. J. Amann, H. N. Higgs, J.-B. Marchand, D. A. Kaiser, and T. D. Pollard, Nature (London) **404**, 1007 (2000).
[26] J. R. Bartles, Curr. Opin. Cell Biol. **12**, 72 (2000).
[27] G. Borisy and T. Svitkina, Curr. Opin. Cell Biol. **12**, 104 (2000).
[28] T. D. Pollard, L. Blanchoin, and R. D. Mullins, Annu. Rev. Biophys. Biomol. Struct. **29**, 545 (2000).
[29] N. Kureishy, V. Sapountzi, S. Prag, N. Anilkumar, and J. C. Adams, BioEssays **24**, 350 (2002).
[30] S. J. Winder, Curr. Opin. Cell Biol. **15**, 14 (2003).
[31] H. N. Higgs and T. D. Pollard, Annu. Rev. Biochem. **70**, 649 (2001).
[32] J. Howard, *Mechanics of Motor Proteins and the Cytoskeleton* (Sinauer Associates, Sunderland, MA, 2001).
[33] T. Svitkina and G. Borisy, Trends Biochem. Sci. **24**, 432 (1999b).
[34] D. Pantaloni, R. Boujemaa, D. Didry, P. Gounon, and M.-F. Carlier, Nat. Cell Biol. **2**, 385 (2000).
[35] D. Vignjevic, S. Kojima, Y. Aratyn, O. Danciu, T. Svitkina, and G. G. Borisy, J. Biol. Chem. **174**, 863 (2006).
[36] A. Mogilner and G. F. Oster, Biophys. J. **84**, 1591 (2003).
[37] M. E. J. Newman and G. T. Barkema, *Monte Carlo Methods in Statisical Physics* (Clarendon Press, Oxford, 1999).
[38] F. Lanni, D. L. Taylor, and B. R. Ware, Biophys. J. **35**, 351 (1981).
[39] J. L. McGrath, Y. Tardy, C. F. J. Dewey, J. J. Meister, and J. H. Hartwig, Biophys. J. **75**, 2070 (1998).
[40] A. van Oudenaarden and J. A. Theriot, Nat. Cell Biol. **1**, 493 (1999).
[41] G. B. Ermentrout and L. Edelstein-Keshet, J. Theor. Biol. **160**, 97 (1993).
[42] A. Troisi, V. Wong, and M. A. Ratner, Proc. Natl. Acad. Sci. U.S.A. **102**, 255 (2005).
[43] H. Y. Lee and M. Kardar, Phys. Rev. E **64**, 056113 (2001).
[44] I. V. Maly and G. G. Borisy, Proc. Natl. Acad. Sci. U.S.A. **98**, 11324 (2001).
[45] A. B. Bortz, M. H. Kalos, and J. L. Lebowitz, J. Comput. Phys. **17**, 10 (1975).
[46] D. T. Gillespie, J. Phys. Chem. **81**, 2340 (1977).
[47] M. Matsumoto and T. Nishimura, ACM Trans. Model. Comput. Simul. **8**, 3 (1998).
[48] D. C. Wylie, Y. Hori, A. R. Dinner, and A. K. Chakraborty, J. Phys. Chem. B **110**, 12749 (2006).
[49] M. A. Gibson and J. Bruck, J. Phys. Chem. A **104**, 1876 (2000).
[50] J. Elf, A. Don, and M. Ehrenberg, Proc. SPIE **5110**, 114 (2003).
[51] R. L. Kruse, B. P. Leung, and C. L. Tondo, *Data Structures and Program Design in C*, 2nd ed. (Prentice-Hall, Upper Saddle River, NJ, 1997).